

Supporting Information: Bioselective Agglutination Induced Nanoscale Deterministic Lateral Displacement

Kuan Yu Hsieh^{a,b,c}, Joshua T. Smith^a, Sung-Cheol Kim^e, Stacey M. Gifford^a, Michael Pereira^a, Guan-Yu Chen^{*b,c,d}, Benjamin H. Wunsch^a

Contents

1	DLD Operating Principles	2
2	Chip Fabrication	4
3	Experimental Setup	6
4	On-Chip Condenser for Focused Injection with Single Fluidic Input	7
5	Fluorescent Image Analysis	8
6	Displacement Efficiency of Particles in Different Buffers	10
7	Agglutination Model	11
7.1	Derivation	11
7.2	Distribution of k-mer clusters	14
8	Parameter Analysis	15
8.1	Influence of Number of Antibodies per Particle in Immunoagglutination	15
8.2	Influence of Number of Particles in Immunoagglutination	15
8.3	Agglutination Dynamics under Constant Total Antibody Concentration	15
8.4	Agglutination Degree over Varying Analyte Concentrations at Different Endpoint Times	17

a IBM T.J. Watson Research Center, 1101 Kitchawan Road, Yorktown Heights, Yorktown, NY 10598, USA
b Department of Electrical and Computer Engineering, College of Electrical and Computer Engineering, National Yang Ming Chiao Tung University, Hsinchu 30010, Taiwan
c Institute of Biomedical Engineering, College of Electrical and Computer Engineering, National Yang Ming Chiao Tung University, Hsinchu 30010, Taiwan
d Department of Biological Science and Technology, National Yang Ming Chiao Tung University, Hsinchu 30010, Taiwan
e Factory Mutual Insurance Co., 270 Central Avenue, Johnston, RI, 02919, USA

1 DLD Operating Principles

The pillar array consists of rows of pillars with diameter D_0 , each of them is placed by a distance D_x along the x-axis, which leaves a gap of G in between. The distance between adjacent rows is defined as D_y ; each row of pillars shifts from the previous row by δ (row-to-row shift), resets laterally to the starting position after every N rows, and yields a row-shift fraction of $\epsilon = \delta/D_x = 1/N$ (N is also known as the array period). The array configuration defines the maximum displacement angle within the array $\theta_{max} = \arctan(\epsilon)$. When $D_x = D_y$, the critical diameter D_C for the system is defined using Equation (1).¹

Particles with a diameter (d_p) greater than a critical diameter (d_c) travel along the *bump mode* trajectory (orange streamline in Figure 1b) and displace laterally (ΔW) towards the wall of the channel along the direction of pillar row shift at θ_{max} , while particles smaller than d_c follow a *zigzag mode* trajectory. In zigzag mode, particles theoretically move in the flow direction without displacing ($\theta = 0^\circ$). Particles can have an intermediate migration angle (θ , where $0^\circ < \theta < \theta_{max}$) (blue region in Figure 1c). This phenomenon has been discussed in several studies.²⁻⁴ Kim *et al.* suggested that the intermediate displacement of particles is due to pseudoperiodicity, which is the average local periodicity of a particle trajectory over multiple cycles.² When the pseudoperiodicity is greater than N , the average direction of the trajectory does not align with the y-axis of the array, resulting in a displacement along $0^\circ < \theta < \theta_{max}$. This is known as an *altered zigzag* trajectory.

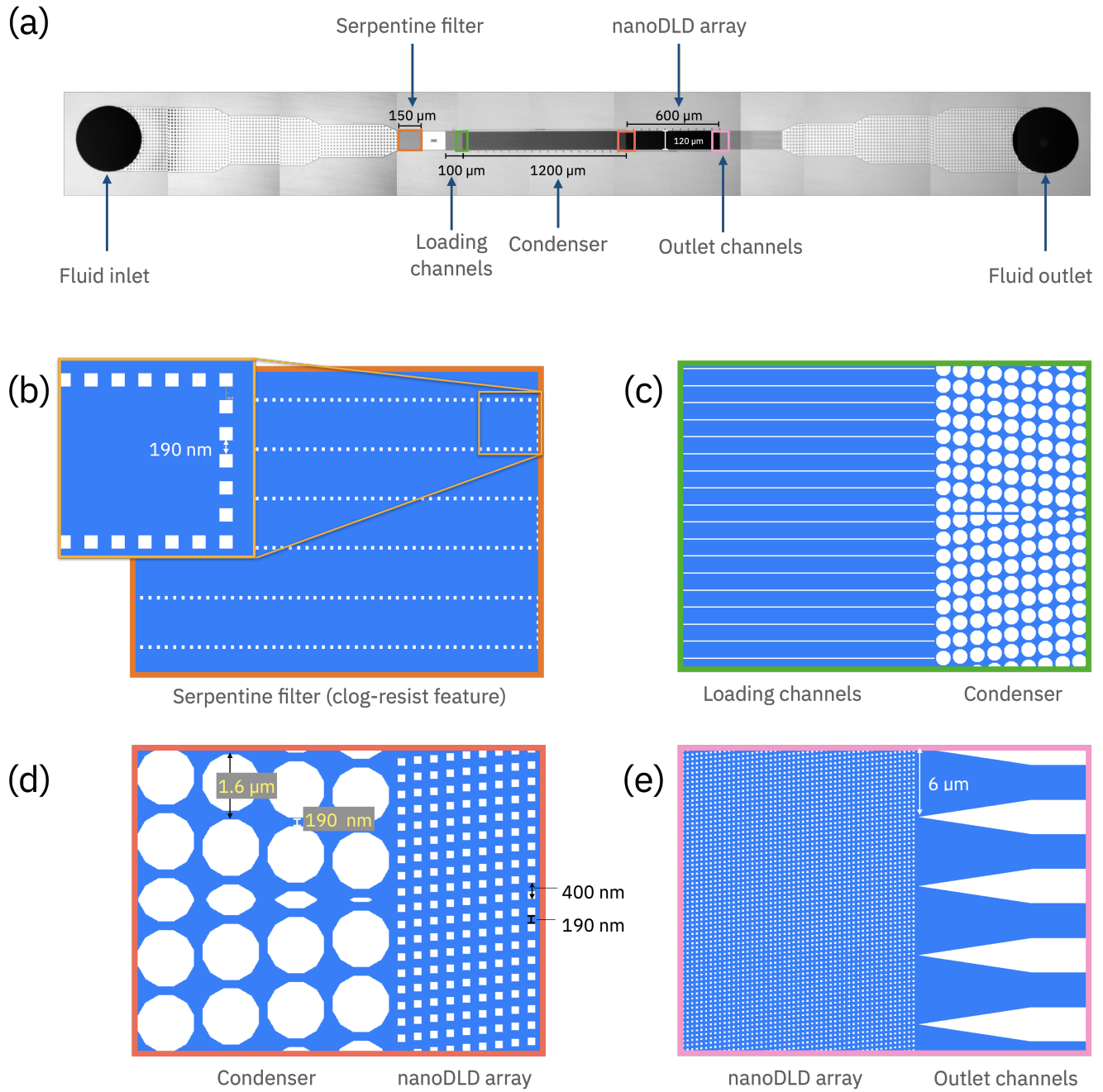


Figure S1: Chip Design. (a) A composite image of whole chip layout, image is assembled by stitching multiple adjacent images together. (b) A zoom-in of the upstream serpentine filter to prevent large particles entering the array in order to increase longevity of the chip. The serpentine filter consists of gaps with the same gap size as the downstream nanoDLD array. (c) Interface of loading channels and condenser array. (d) Interface of condenser array and nanoDLD array. Condenser array and nanoDLD array has the same gap size, while the pitch size in condenser array is 4 times of the nanoDLD array. Condenser is made up of 2 arrays that mirror towards center, nanoDLD array is tilted right. (e) nanoDLD outlet is divided to 20 outlet channels.

2 Chip Fabrication

Chips (20 mm \times 15 mm) were fabricated for this study, having a L1 = 1.2 mm upstream condenser array used for focusing particle streams toward the center of the array width $W = 120 \mu\text{m}$ that feed the downstream L2 = 0.6 mm nanoDLD array having $G \approx 200 \text{ nm}$ and $P = 400 \text{ nm}$ with the same array width. Pillar arrays and other shallower microfluidic features (filters, pre-array loading features, outlet microchannels, etc.) were defined using 193-nm lithography and reactive-ion etching (RIE) scheme.

Feature Patterning. Prior to resist coating, 200-mm silicon wafers were RCA cleaned and a 300 nm-thick SiO_2 layer was grown on the surface to provide a hard mask (HM) for pillar array definition during RIE processing. Next, a tri-layer stack was spin coated onto the wafers to prepare them for lithographic exposure, which included a 500 nm HM8006 organic planarization layer (OPL) (JSR Microelectronics), a 70 nm SHBA-940-L35 Si-containing anti-reflective coating (Si ARC) (Shin-Etsu MicroSi, Inc., AZ), and finally a 160 nm-thick positive tone AR1570-16-35SD resist. A 0.75 NA 193-nm wavelength step-and-scan PAS 5500/1100 B-4X scanner system (ASML) was used to expose the resist layer at a dose and focus 14 mJ and 0 μ , respectively, to achieve $G = 190 \text{ nm}$.

Feature Etching. After developing the exposed wafers, downstream RIE was used to selectively transfer the exposed pattern into silicon. Pillar definition was carried out in a DPSII ICP etch chamber (Applied Materials, CA) using a 5-step process to etch pillars to a depth of $\approx 1 \mu\text{m}$: (1) Si ARC breakthrough was achieved using an CF_4/CHF_3 chemistry at 500 W source power, 100 W bias power and 30 mTorr pressure at 65 C; (2), an $\text{N}_2/\text{O}_2/\text{Ar}/\text{C}_2\text{H}_4$ chemistry at 400 W source power, 100W bias power, and 4 mTorr pressure at 65 C was then applied to break through the OPL; (3) the pattern was defined in the SiO_2 HM using the same conditions and chemistry applied during the step (1) Si ARC etch. Steps (1) – (3) utilized end-point (EP) detection as a quality control (QC) affirmation of material breakthrough with etch times adjusted around EP for each wafer to ensure reproducibility; (4) After HM patterning, the OPL carbon resist was stripped in an Axiom downstream asher (Applied Materials, CA) using an O_2/N_2 chemistry; (5) involved transferring the HM pattern into silicon. This was accomplished using the DPS II ICP etch system (Applied Materials, CA) by applying a 5 sec $\text{CF}_4/\text{C}_2\text{H}_4$ native oxide open RIE followed by a $\text{Cl}_2/\text{HBr}/\text{CF}_4/\text{He}/\text{O}_2/\text{C}_2\text{H}_4$ main etch using 650 W source power, 85W bias power, and 4 mTorr pressure at 65°C to etch all features to a depth of $\approx 1 \mu\text{m}$.

Post-Etch Cleans and Bonding Prep. After RIE etching to define the integrated nanoDLD pillar arrays, residual organics were removed in a bath containing a 10:1 mixture of sulfuric/nitric acid at 150 C, after which the HM was removed completely in a 10:1 dilute hydrofluoric (DHF) acid bath. The wafers were then cleaned in a 3-step process, including a 10 min piranha clean (5:1 volume ratio of 98% H_2SO_4 and 30% H_2O_2) to remove organic residue, 60 sec 100:1 DHF dip to remove any native oxide formed, and an SC1 clean (1:1:5 H_2O_2 : NH_4OH :deionized water (DI)) at 65°C with intermittent rinse steps.

A subsequent RCA clean prepared wafers for a thin thermal oxide growth of 5 nm of SiO_2 , which simultaneously prepared the substrate for subsequent anodic bonding. Borosilicate glass wafers (Swift Glass, NY) with a measured thickness of $\sim 700 \mu\text{m}$ were SC1 cleaned (1:1:5 H_2O_2 : NH_4OH :DI) for 10 min at 65°C and spin-rinse-dried (SRD) to prepare them for bonding to the silicon wafers.

Anodic Bonding. A Süss SB6 anodic bonder (Süss MicroTech) was used to bond the borosilicate glass wafers to the silicon wafers. A CL200 megasonic clean was applied to both bonding surfaces prior to the bonding process. For this, DI water was dispensed through a 1 MHz megasonic nozzle to further clean the bonding surfaces, a process followed by a spin dry to remove any water on the surface. Anodic bonding was carried out in a 0.005 mbar N_2 environment at 260°C with a voltage of -600 V and down force = 1100 mbar applied to the wafer stack for 9 minutes.

Silicon Polishing. After monolithically bonding the glass and silicon wafers, the silicon was thinned and polished from the unbonded side to a thickness of $\sim 150 \mu\text{m}$ in a 2-stage chemical mechanical polish (CMP) process. A course silicon grind was accomplished using a DAG810 Automatic In-Feed Surface Grinder (DISCO Corporation, Japan) to thin bulk silicon, removing $\sim 540 \mu\text{m}$ of the nominally 725 μm -thick silicon wafer followed by a post grind cleaning in DCS1440 Disco Cleaning System (DISCO Corporation, Japan), and a final 35 μm polish in an IPEC-Westech 372M (Axus Technology, AZ) was utilized for post-grind CMP to meet final thickness and surface quality targets by applying Nalco 2358, a colloidal silica abrasive slurry, to polish the silicon to a $\sim 100 \mu\text{m}$ final thickness and a mirror-like surface finish. A brush clean with oxalic acid and rinse was used to clean the wafers after polish as well as a downstream SRD to ensure the removal of slurry particles.

TSV Patterning and Open. Fluidic access points for routing fluid to and from the integrated nanoDLD chips from

the backside of the chips were formed. A 3 μm -thick layer of TOKip 3250-27 cp resist (Tokyo) was applied to the polished silicon and an optical contact MA8 mask aligner (Karl Suss, Germany) with front-to-back alignment was used to pattern the via positions. The open pattern features were used to etch the vias with a deep silicon RIE process. Deep silicon etching was achieved with an Alcatel 601E inductively coupled plasma etcher (Alcatel Micro Machining Systems, France) using a Bosch process with alternating pulses of SF_6 300 sccm and C_4F_8 150 sccm at a temperature of 20°C with source and bias powers of 1800 W and 80 W, respectively. Via breakthrough was verified visually with backlighting and with an optical microscope. An O_2 ash system (Plasma-Therm, FL) was used to remove resist from the silicon wafer after RIE. Wafers were subsequently diced while attached to a high-tack dicing film to prevent liquid from wetting the chips before use. This process resulted in 72 usable chips per wafer.

3 Experimental Setup

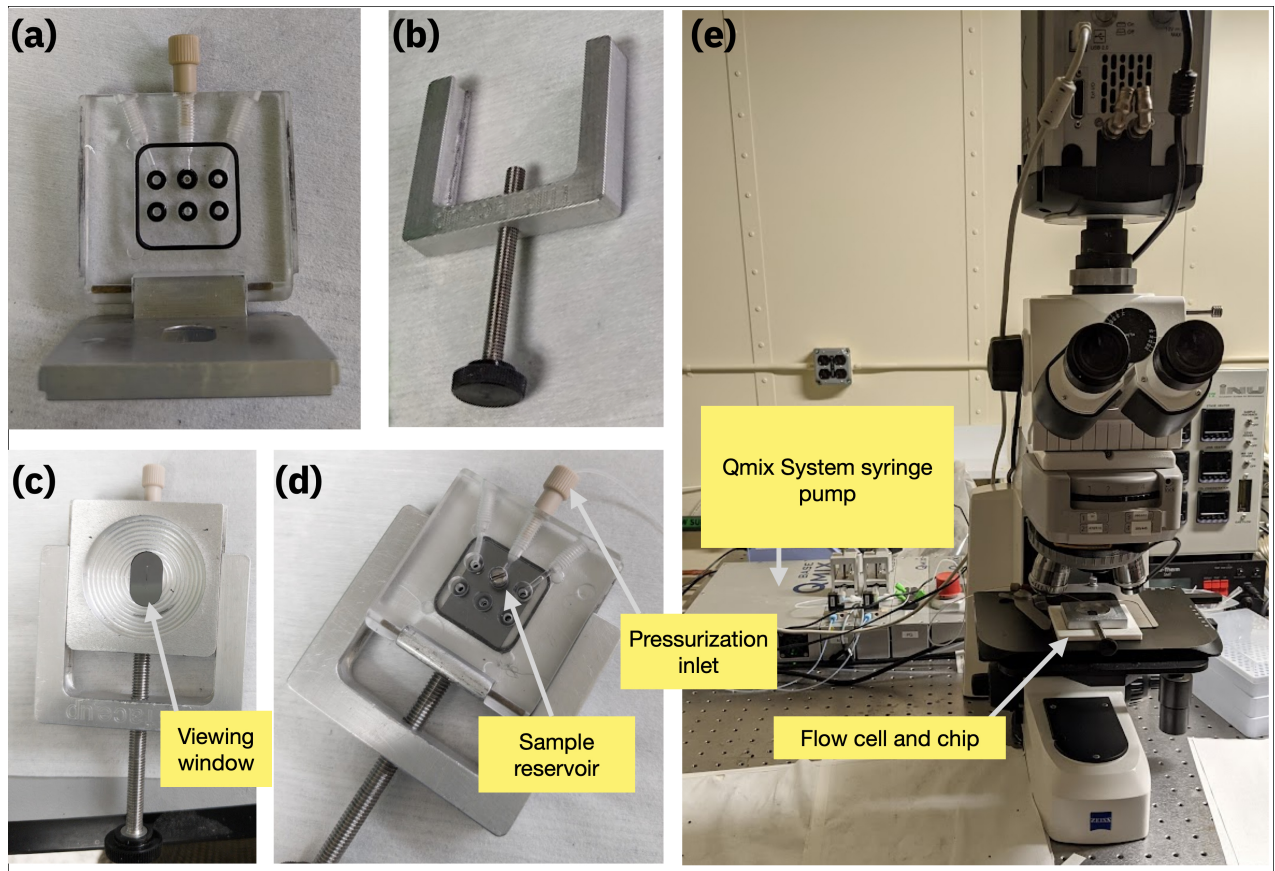


Figure S2: Experimental Setup for nanoDLD Chip Operation and Fluorescent Microscopy Imaging. (a) Custom-built flow cell to hold the chip. (b) The mounting base to secure and position the chip. (c) The mounting base secures the chip-loaded flow cell, a transparent viewing window for microscopy imaging. (d) The sample reservoir aligns with the chip's pressurization inlet. (e) Overall setup with the fluorescence microscope and the Qmix System syringe pump.

4 On-Chip Condenser for Focused Injection with Single Fluidic Input

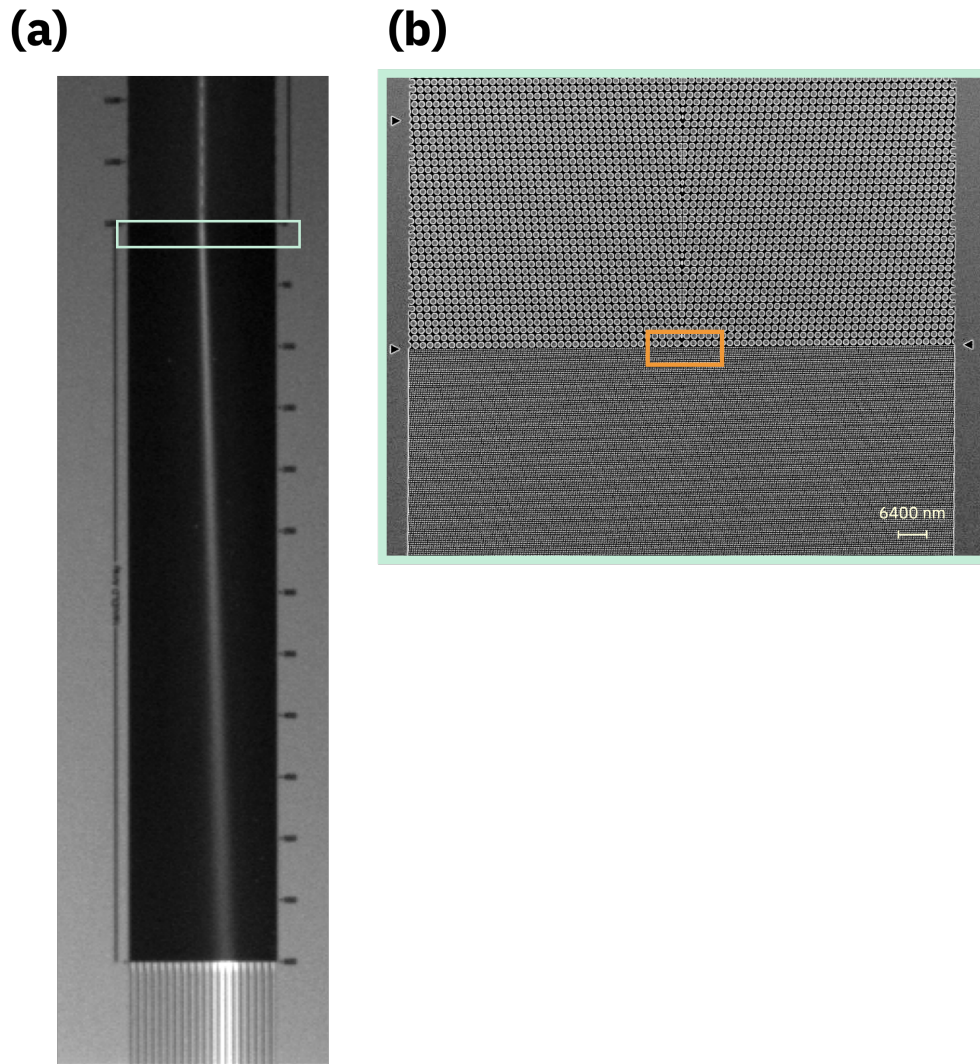


Figure S3: (a) An overview of the upstream condenser and the nanoDLD array. Streamline is from the fluorescent signal from the particles. The green box indicates the interface of the condenser and nanoDLD array. Particles are focused towards the center along the condenser array and deflect to displace laterally along the nanoDLD array. (b) A close-up SEM image of the condenser's mirrored DLD arrays. The intricate pillar structures are evident, with the larger pillars of the condenser ($D_{0,condenser} = 1410$ nm) contrasted against the smaller pillars of the nanoDLD array ($D_{0,nanoDLD} = 210$ nm). Both arrays have the same pillar arrangement and gap size of $G \approx 190$ nm

5 Fluorescent Image Analysis

Fluorescence images from a 200-frame video were first stacked into one image, then x-coordinate of the fluidic channel wall (cyan line in (Figure S4a)) and the injection point (pink line in (Figure S4a)) of nanoDLD were identified in the stacked image. The x-coordinate (pixel) is converted to the lateral position (μm) based on the geometry of the chip (Figure S4b).

To determine the displacement efficiency, a line profile along the nanoDLD outlet was extracted and smoothed by applying a Savitzky-Golay filter. The distance between the peak from the outlet line profile and the x-coordinate of the injection point equals the lateral displacement (ΔW). The displacement efficiency can be calculated by Equation S1, and the migration angle can be determined by $\theta = \tan^{-1}(\Delta W L^{-1})$.

$$\eta = \frac{dW}{W} = \frac{\tan \theta}{\tan \theta_{\max}} \sim \frac{\theta}{\theta_{\max}} \quad (\text{S1})$$

To determine the signal ratio, when fluorescent signal line profile across the outlet channels were extracted and mapped to their lateral position (μm), the two right-most channels (orange region in Figure S4b) are the outlets for particles in bump mode, and particles follow zigzag trajectory exit the array within the channels in purple in Figure S4b. As the aggregation ratio is defined as Equation S2, it could be yielded by dividing the fluorescent intensity in bump outlet channels (area under curve of orange region) by the total fluorescent intensity in all 10 outlet channels (area under curve of orange and purple region in Figure S4b).

$$\text{Signal ratio} = \frac{I_{\text{bump}}}{I_{\text{bump}} + I_{\text{zigzag}}} \quad (\text{S2})$$

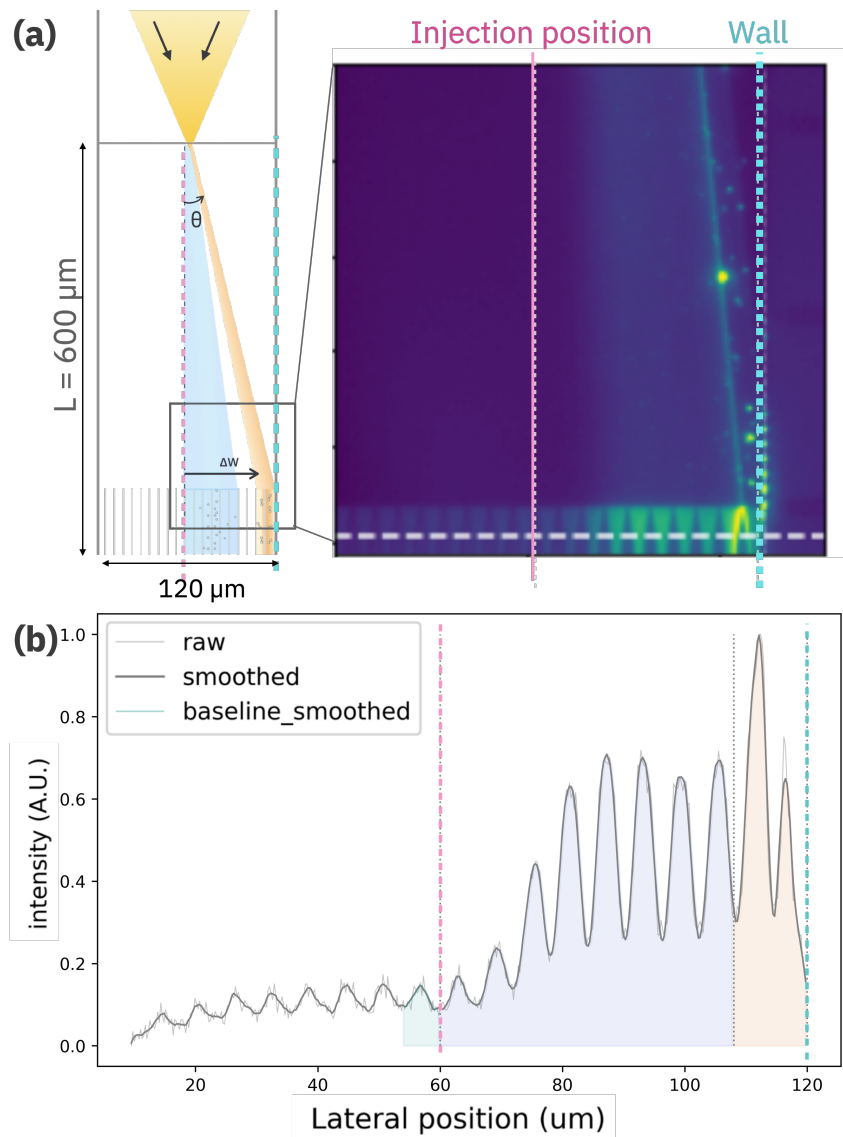
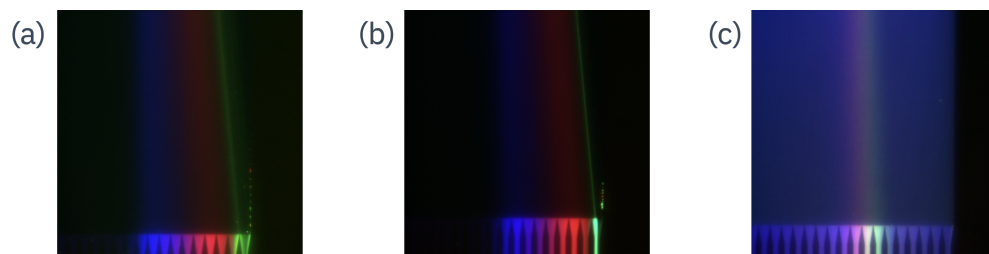


Figure S4: Image analysis for nanoDLD system to determine displacement efficiency and aggregation ratio. (a) The composite fluorescence image from a stacked 200-frame video indicates the fluidic channel's wall (cyan line) and the nanoDLD injection point (pink line). The particles displace laterally for ΔW as they navigate the channel. (b) Intensity line profile acquired along the nanoDLD outlet (raw, Savitzky-Golay filter smoothed, and baseline-smoothed results). The lateral position is converted from pixels to micrometers (μm) to align with the chip's geometry. The regions highlighted in orange and purple represent the bump mode outlet channels and the zigzag trajectory outlet channels.

6 Displacement Efficiency of Particles in Different Buffers



Buffer	DI H ₂ O	0.001x PBS	PBS
Ionic concentration	0	167 μ M	167 mM
Operating pressure (bar)	8 bar	8 bar	8 bar
Displacement Efficiency (%)	20 nm beads: 21.32%	20 nm beads: 23.87%	20 nm beads: 5.62%
	40 nm beads: 60.76%	40 nm beads: 65.41%	40 nm beads: 22.60%
	75 nm beads: 90.32%	75 nm beads: 92.85%	75 nm beads: 31.1%

Figure S5: Ionic concentration of buffer affects displacement efficiency. Comparison of particle displacement efficiency under different buffer conditions: (a) Deionized (DI) water with an ionic concentration of 0 M, (b) 0.001x PBS with an ionic concentration of 167 μ M, and (c) 1xPBS with an ionic concentration of 167 mM. All experiments were operated at 8 bar pressure.

7 Agglutination Model

7.1 Derivation

The following section closely follows the derivation previously presented⁵ to yield the reaction model discovered earlier⁶. Based on Smoluchowski's coagulation equation⁷, a general time-dependent dynamics of concentration of k -mer cluster (cluster that consists of k particles) can be expressed as

$$\frac{dn(k, t)}{dt} = \frac{1}{2} \sum_{\substack{j=1 \\ j+l=k}}^{k-1} R_{jl} n_j n_l - n_k \sum_{j=1}^{\infty} R_{kj} n_j \quad (\text{S3})$$

where the first term is the formation of k -mer clusters, R_{jl} is the reaction rate between j -mer clusters and l -mer clusters, n_j and n_l are the concentration of j - and l -mer clusters respectively. The second term is the loss of k -mer clusters, in which R_{kj} is the reaction rate between k -mer clusters and j -mer clusters, n_j and n_k are the concentration of j - and k -mer clusters respectively.

According to the reaction model presented previously^{5,6}, during the immunoagglutination process, the time-dependent concentration of free analyte can be expressed as

$$\frac{dn_l(t)}{dt} = -C_2 n_l(t) [1 - a(t)] f N_p + C_3 a(t) f N_p \quad (\text{S4})$$

where n_l is the concentration of free analyte (M), C_2 and C_3 is the analyte-antibody binding ($M^{-1}s^{-1}$) and dissociate rate constant (s^{-1}) respectively. $a(t)$ is the time-dependent occupied antibody fraction. N_p is the initial concentration of particles (M), f is the number of antibodies per particle, thus $f \times N_p$ is the total concentration of antibody (M). The first term represents the free analyte during analyte-antibody binding reaction, $[1 - a(t)]$ is the free antibody fraction, and $[1 - a(t)] f N_p$ is the concentration of free antibody (M); the second term is the free analyte concentration during analyte-antibody dissociation.

Time-dependent occupied antibody fraction is

$$\frac{da(t)}{dt} = C_2 n_l(t) [1 - a(t)] - C_3 a(t) \quad (\text{S5})$$

where the first term represents the free analyte binds to the free antibody, and the second term denotes the dissociation of analyte-antibody complex. By substituting Equation S5 to Equation S4, time-dependent concentration of free analyte can be expressed as

$$\frac{dn_l(t)}{dt} = -f N_p \frac{da(t)}{dt} \quad (\text{S6})$$

Let N_l be the analyte concentration (M), and $s = \frac{N_p f}{N_l}$, Equation S6 becomes

$$\frac{dn_l(t)}{dt} = -s N_l \frac{da(t)}{dt} \quad (\text{S7})$$

Next, integrate both Equation S7 on both side,

$$\int \frac{dn_l(t)}{dt} dt = -s N_l \int \frac{da(t)}{dt} dt \quad (\text{S8})$$

which yields

$$n_l(t) = -s N_l a(t) + C \quad (\text{S9})$$

At $t = 0$, since no reaction occurs, all analyte molecules are free analyte, thus $n_l = N_l$, and $a(0) = 0$,

$$N_l = -s N_l \times 0 + C \quad (\text{S10})$$

therefore $C = N_l$. This results in

$$n_l(t) = -s N_l a(t) + N_l \quad (\text{S11})$$

and can be reorganized into

$$n_l(t) = N_l[1 - sa(t)] \quad (\text{S12})$$

Substitute Equation S12 to Equation S5,

$$\frac{da(t)}{dt} = C_2 N_l [1 - sa(t)][1 - a(t)] - C_3 a(t) \quad (\text{S13})$$

$$\frac{da(t)}{dt} = C_2 N_l [sa^2(t) - a(t)(1 + s) + 1] - C_3 a(t) \quad (\text{S14})$$

$$\frac{da(t)}{dt} = C_2 N_l [sa^2(t) - a(t)(1 + s + \frac{C_3}{C_2 N_l}) + 1] \quad (\text{S15})$$

Let $\alpha = \frac{C_3}{C_2 N_l}$, and the time-dependent dynamics of occupied antibodies fraction can be expressed as

$$\frac{da(t)}{dt} = C_2 N_l [sa^2(t) - a(t)(1 + s + \alpha + 1)] \quad (\text{S16})$$

To tailor this equation for the immunoagglutination process, reaction parameters were introduced into Equation S3, including agglutination rate constant (C_1) and $a(t)$. This gives the time-dependent concentration of k -mer clusters during immunoagglutination to be

$$\frac{dn(k, t)}{dt} = C_1 a(t) [1 - a(t)] \left[\frac{1}{2} \sum_{j=1}^{k-1} n(j, t)n(k-j, t) - n(k, t) \sum_{j=1}^{\infty} [n(j, t)] \right] \quad (\text{S17})$$

Let $N(t)$ be total concentration of clusters (i.e. monomers + dimers + trimers + ... + k -mers)

$$N(t) = \sum_{k=1}^{\infty} n(k, t) \quad (\text{S18})$$

and sum both sides of Equation S17 from $k = 1$ to ∞ :

$$\sum_{k=1}^{\infty} \frac{dn(k, t)}{dt} = \sum_{k=1}^{\infty} \left[C_1 a(t) [1 - a(t)] \times \left\{ \frac{1}{2} \sum_{\substack{j=1 \\ j+l=k}}^{k-1} [n(j, t)n(l, t)] - n(k, t) \sum_{j=1}^{\infty} [n(j, t)] \right\} \right] \quad (\text{S19})$$

Left-hand side becomes

$$\sum_{k=1}^{\infty} \frac{dn(k, t)}{dt} = \frac{d \sum_{k=1}^{\infty} n(k, t)}{dt} = \frac{dN(t)}{dt} \quad (\text{S20})$$

On the right-hand side, the construction of k -mer clusters is half of the following expression to avoid double counting as the order of formation is assumed to have no effects on coagulation⁸.

$$\sum_{k=1}^{\infty} \sum_{\substack{j=1 \\ j+l=k}}^{k-1} [n(j, t)n(l, t)] \quad (\text{S21})$$

$$= \sum_{k=1}^{\infty} \sum_{\substack{j=1 \\ j+l=k}}^{k-1} [n(j, t)n(k-j, t)] \quad (\text{S22})$$

Omitting t , Equation S22 becomes

$$\sum_{k=1}^{\infty} [n(1)n(k-1) + n(2)n(k-2) + \dots + n(k-2)n(2) + n(k-1)n(1)] \quad (\text{S23})$$

$$\begin{aligned}
&=n(1)n(0) + n(2)n(-1) + n(3)n(-2) + n(4)n(-3) + \dots \\
&\quad + n(1)n(1) + n(2)n(0) + n(3)n(-1) + n(4)n(-2) + \dots \\
&\quad + n(1)n(2) + n(2)n(1) + n(3)n(0) + n(4)n(-1) + \dots \\
&\quad + n(1)n(3) + n(2)n(2) + n(3)n(1) + n(4)n(0) + \dots \\
&\quad + n(1)n(4) + n(2)n(3) + n(3)n(2) + n(4)n(1) + \dots \\
&\quad + \dots
\end{aligned}$$

Since cluster at least contains one particle $k \geq 1$; for $k < 1$, $n(k) = 0$

$$\begin{aligned}
&=n(1) \cdot 0 + n(2) \cdot 0 + n(3) \cdot 0 + n(4) \cdot 0 + \dots \\
&\quad + n(1)n(1) + n(2) \cdot 0 + n(3) \cdot 0 + n(4) \cdot 0 + \dots \\
&\quad + n(1)n(2) + n(2)n(1) + n(3) \cdot 0 + n(4) \cdot 0 + \dots \\
&\quad + n(1)n(3) + n(2)n(2) + n(3)n(1) + n(4) \cdot 0 + \dots \\
&\quad + n(1)n(4) + n(2)n(3) + n(3)n(2) + n(4)n(1) + \dots \\
&\quad + \dots \\
&=n(1)n(1) \\
&\quad + n(1)n(2) + n(2)n(1) \\
&\quad + n(1)n(3) + n(2)n(2) + n(3)n(1) + \dots \\
&\quad + n(1)n(4) + n(2)n(3) + n(3)n(2) + n(4)n(1) \dots \\
&=n(1)[n(1) + n(2) + n(3) + n(4) + \dots] \\
&\quad + n(2)[n(1) + n(2) + n(3) + \dots] \\
&\quad + n(3)[n(1) + n(2) + \dots] + \dots \\
&\quad + n(4)[n(1) + \dots] + \dots \\
&= \sum_{j=1}^{\infty} n(j) \cdot \sum_{l=1}^{\infty} n(l)
\end{aligned}$$

Thus, the construction of k -mer clusters is

$$\frac{1}{2} \sum_{k=1}^{\infty} \sum_{\substack{j=1 \\ j+l=k}}^{k-1} [n(j, t)n(l, t)] = \frac{1}{2} \sum_{j=1}^{\infty} n(j) \cdot \sum_{l=1}^{\infty} n(l) \quad (\text{S24})$$

and the lost of k -mer clusters is

$$\sum_{k=1}^{\infty} n(k, t) \sum_{j=1}^{\infty} n(j, t) \quad (\text{S25})$$

By combining Equation S24 and Equation S25:

$$\frac{dN(t)}{dt} = C_1 a(t) [1 - a(t)] \times \left[\frac{1}{2} \sum_{j=1}^{\infty} n(j, t) \cdot \sum_{l=1}^{\infty} n(l, t) - \sum_{k=1}^{\infty} n(k, t) \sum_{j=1}^{\infty} n(j, t) \right] \quad (\text{S26})$$

Substitute $N(t) = \sum_{k=1}^{\infty} n(k, t)$,

$$\frac{dN(t)}{dt} = C_1 a(t) [1 - a(t)] \times \left[\frac{1}{2} N(t) \cdot N(t) - N(t) \cdot N(t) \right] = C_1 a(t) [1 - a(t)] \times \left[-\frac{1}{2} N^2(t) \right] \quad (\text{S27})$$

Therefore, the time-dependent dynamics of the total concentration of clusters is

$$\frac{dN(t)}{dt} = C_1 a(t) [1 - a(t)] \times \left[-\frac{1}{2} N^2(t) \right] \quad (\text{S28})$$

The rate of change of the number of particles, $\frac{dN(t)}{dt}$, is always negative since particles combine to form larger clusters as time passes, resulting in a decrease in the total concentration of clusters.

To express the fraction of particles involved in agglutination, which is the particles involved in the formation of clusters, let $A(t)$ be the normalized particle agglutination degree, and $0 < A(t) \leq 1$

$$A(t) = \frac{N(t)}{N_p} \quad (\text{S29})$$

Multiply $\frac{1}{N_0}$ to both side of Equation S28,

$$\frac{1}{N_p} \times \frac{dN(t)}{dt} = C_1 a(t) [1 - a(t)] \times \left[-\frac{1}{2} N^2(t)\right] \times \frac{1}{N_p} \quad (\text{S30})$$

Substitute $A(t)$ to LHS,

$$\frac{dA(t)}{dt} = C_1 a(t) [1 - a(t)] \left(-\frac{1}{2} \frac{N^2(t)}{N_p}\right) \quad (\text{S31})$$

and rearrange

$$\frac{dA(t)}{dt} = C_1 N_p a(t) [1 - a(t)] \left(-\frac{1}{2} \frac{N^2(t)}{N_p^2}\right) \quad (\text{S32})$$

Time-dependent dynamics of normalized particle agglutination degree is defined as

$$\frac{dA(t)}{dt} = C_1 N_p a(t) [1 - a(t)] \left(-\frac{1}{2} A^2(t)\right) \quad (\text{S33})$$

The parameters used in this study were defined as follows: C_1 is calculated as C_{1n}/N_0 , where C_{1n} was set to 0.01 s^{-1} based on the previous study⁶, and $N_0 = 1.613 \times 10^{-9} \text{ (M)}$ from our experimental initial particle concentration; C_2 and C_3 was set to $10^7 \text{ (M}^{-1}\text{s}^{-1})$ and $10^{-6} \text{ (s}^{-1})$ respectively according manufacturer's suggestions.

7.2 Distribution of k-mer clusters

A set of coupled differential equations, derived from Equation S17 was solved using Euler's method. This enabled us to calculate the quantity of each k-mer cluster, ranging from monomers to octamers, at different selected analyte concentrations (Figure S6).

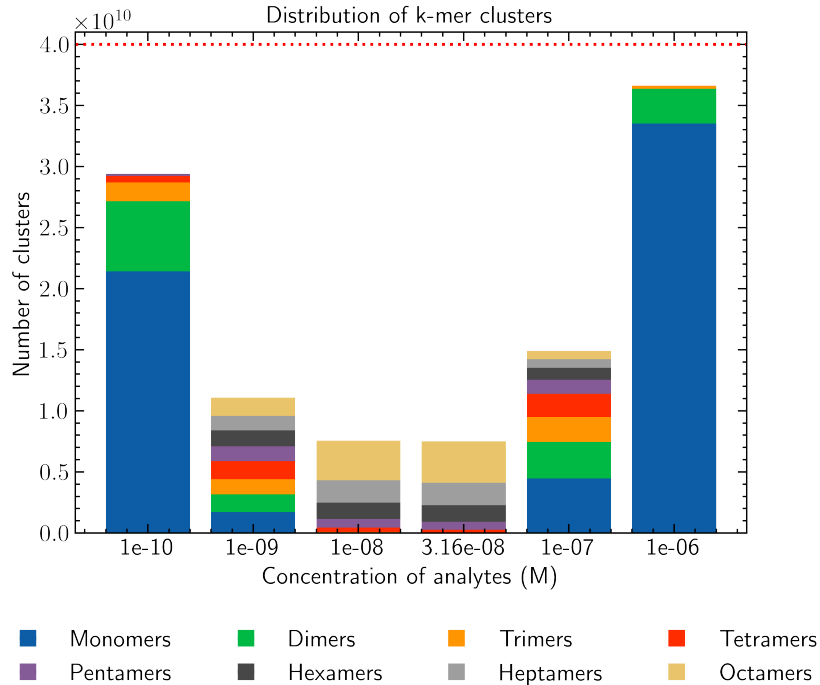


Figure S6: Each bar represents the cluster distribution across selected analyte concentrations. Total bar chart height reflects the total counts of clusters. Each color band denotes different cluster types.

8 Parameter Analysis

To further understand how each parameter affects the model output and find the optimal condition for detection, a sensitivity analysis for each parameter of the model was conducted.

8.1 Influence of Number of Antibodies per Particle in Immunoagglutination

f and N_p have the greatest impact on the model output. Applying this finding to our immunoagglutination process model, we found that a lower number of antibodies per particle, f (Figure S7) or a lower number of particles N_p (Figure S8) shifts the peak of agglutination to a lower analyte concentration. As shown in Figure S7b, we observed variation in the number of antibodies conjugated on each particle affects the agglutination peak position: with a lower f (orange curve in Figure Figure S7b), the peak agglutination occurs at lower analyte concentrations when compared to a higher f (green curve in Figure S7b). In addition, a reduced antibody availability instigates a shift of the antibody excess zone to lower analyte concentrations.

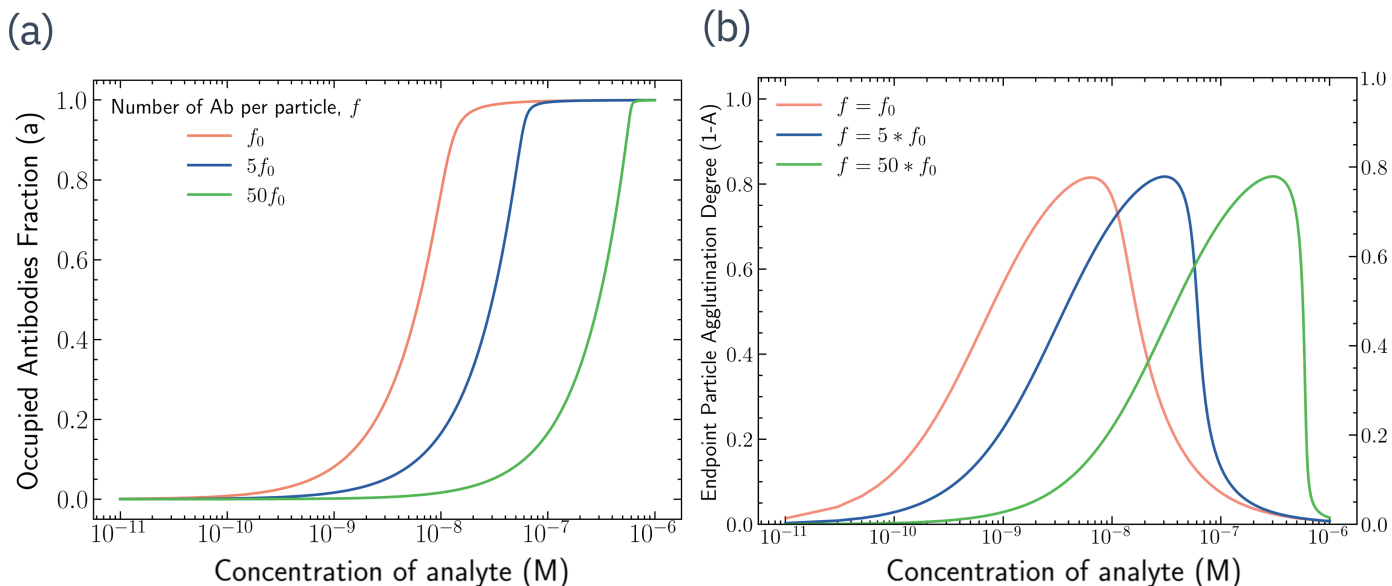


Figure S7: (a) Occupied antibody fraction for varying antibody counts per particle at $t=3600$ s. (b) Agglutination degree with adjusted binding sites by altering f . Lower f (orange curve) results in peak agglutination at decreased analyte concentration compared to higher f (green curve).

8.2 Influence of Number of Particles in Immunoagglutination

Lowering N_p similarly causes a shift of the peak towards diminished analyte concentration. However, this yields a lower agglutination degree when compared to the higher particle concentration (Figure S8). Given our system sensitivity also relies on the fluorescence signal from the particles, varying particle count is not deemed as an optimal approach for adjusting the detection range, as it could lead to challenges in observation and image analysis associated with reduced particle numbers.

8.3 Agglutination Dynamics under Constant Total Antibody Concentration

Furthermore, we simulated the agglutination degree using a constant total antibodies concentration ($f \times N_p$) (Figure S9). Here, we adjusted the number of antibodies per particle in parallel to the concentration of particles. We observed that the peak of agglutination always happens when half of the antibodies are occupied, resulting in different agglutination degrees. This phenomenon can be attributed to the kinetics of bead-based assays, where the concentration and distribution of particles influence reaction rates and binding affinities. The variability in agglutination degrees underlines the intricate interplay between particle concentration and antibody availability, each serving as a critical determinant of reaction dynamics and, consequently, detection sensitivity.

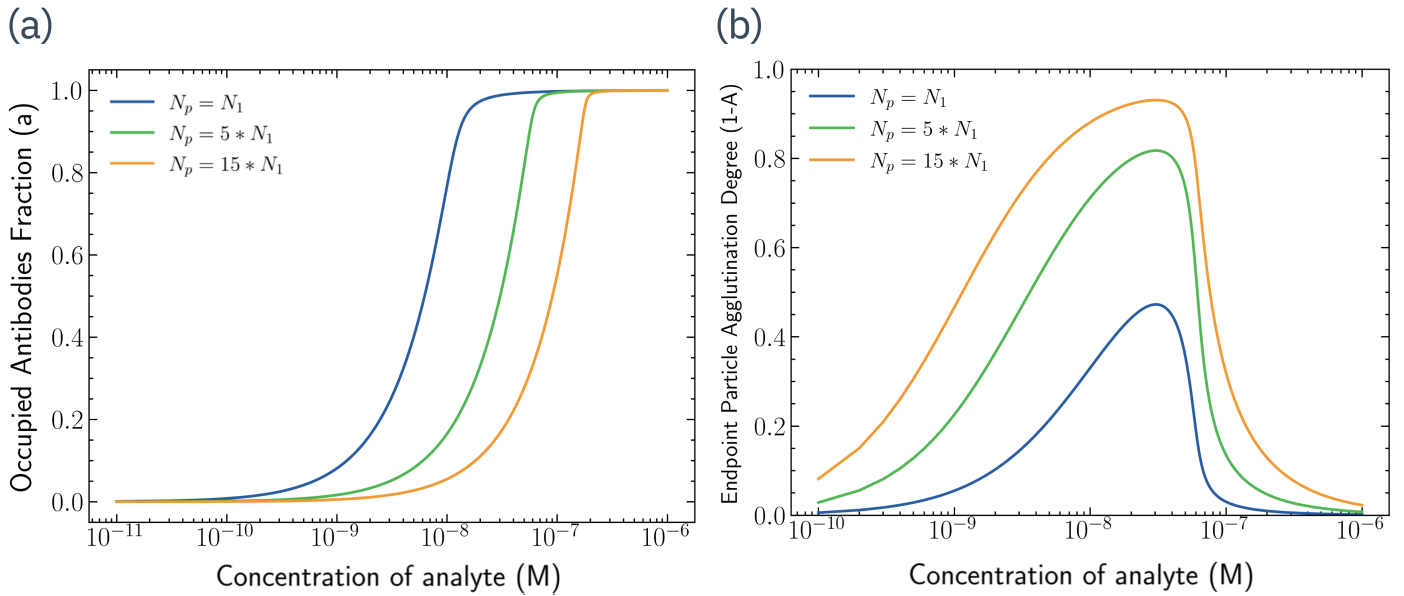


Figure S8: Influence of Number of Particles in Immunoagglutination. (a) Occupied antibody fraction at $t=3600$ s for different values of N_p . (b) Particle agglutination degree across varying analyte concentrations under distinct particle counts. As N_p decreases (orange and green curves), the peak shifts to lower analyte concentrations but with diminished agglutination degree.

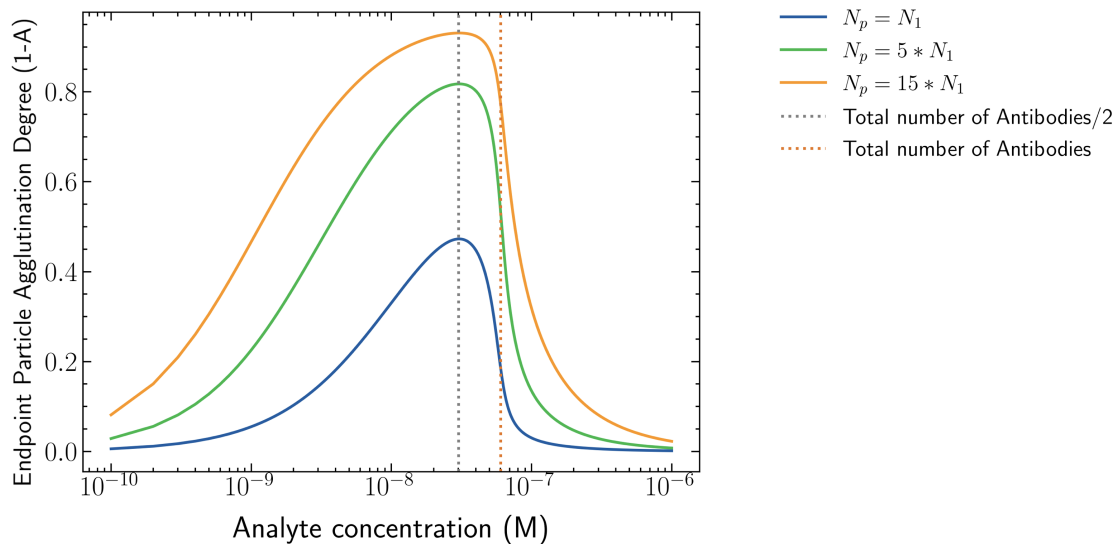


Figure S9: Agglutination Dynamics under Constant Total Antibody Concentration. Simulation demonstrates the agglutination degree with constant total antibodies ($f \times N_p$). The agglutination peaks when half the antibodies are occupied with varying agglutination ratio magnitudes for each condition.

8.4 Agglutination Degree over Varying Analyte Concentrations at Different Endpoint Times

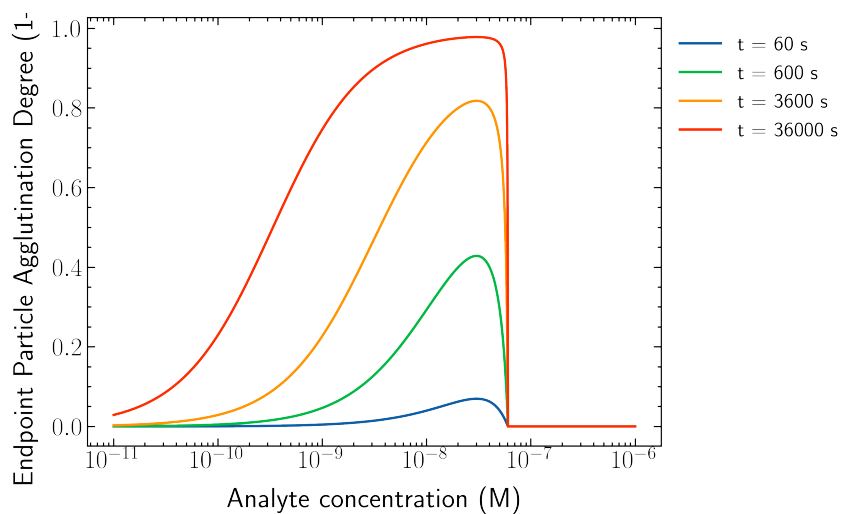


Figure S10: Agglutination Degree over varying analyte concentrations at different endpoint times: 60 seconds (blue), 600 seconds (green), 3600 seconds (orange), and 36,000 seconds (red). The longer the incubation time, the higher the agglutination degree is for the same analyte concentration. All curves peak at the same analyte concentration.

References

- [1] B. H. Wunsch, J. T. Smith, S. M. Gifford, C. Wang, M. Brink, R. L. Bruce, R. H. Austin, G. Stolovitzky and Y. Astier, *Nat. Nanotechnol.*, 2016, **11**, 936–940.
- [2] S.-C. Kim, B. H. Wunsch, H. Hu, J. T. Smith, R. H. Austin and G. Stolovitzky, *Proc. Natl. Acad. Sci. U. S. A.*, 2017, **114**, E5034–E5041.
- [3] T. C. T. A. Heller and H. B. . Micromech. Microeng.
- [4] E. Pariset, C. Pudda, F. Boizot, N. Verplanck, J. Berthier, A. Thuairé and V. Agache, *Small*, 2017, **13**, year.
- [5] N. Kylilis, P. Riangrunroj, H.-E. Lai, V. Salema, L. Fernández, G.-B. V. Stan, P. S. Freemont and K. M. Polizzi, *ACS Sens*, 2019, **4**, 370–378.
- [6] E. B. Dolgosheina, A. Y. Karulin and A. V. Bobylev, *Math. Biosci.*, 1992, **109**, 1–10.
- [7] M. V. Smoluchowski, *Z. Angew. Phys.*, 1916, **17**, 557–585.
- [8] J. A. D. Wattis, *Physica D*, 2006, **222**, 1–20.